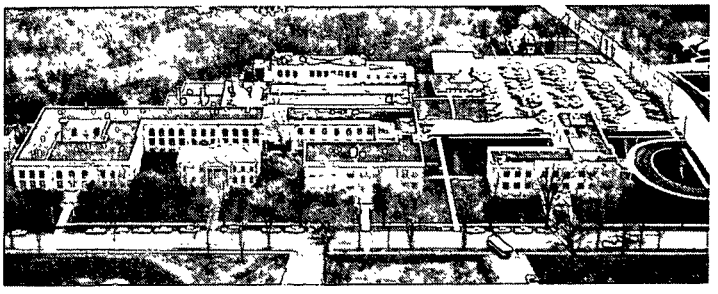

THE INSTITUTE OF PAPER CHEMISTRY, APPLETON, WISCONSIN

IPC TECHNICAL PAPER SERIES

NUMBER 300

IN-SITU FUME PARTICLE SIZE AND NUMBER DENSITY MEASUREMENT FROM SYNTHETIC SMELT

JAY C. L. HSU, DAVID T. CLAY, AND CARY PRESSER

AUGUST, 1988

In-Situ Fume Particle Size and Number Density Measurement from Synthetic Smelt

Jay C. L. Hsu, David T. Clay, and Cary Presser

This manuscript is based on results of IPC research and has been submitted for consideration for publication in Pulp and Paper Science

IN-SITU FUME PARTICLE SIZE AND NUMBER DENSITY MEASUREMENT FROM SYNTHETIC SMELT

Jay C. L. Hsu*

David T. Clay
The Institute of Paper Chemistry
P.O. Box 1039
Appleton, WI 54912

and

Cary Presser
Chemical Process Metrology Division
Center for Chemical Engineering
National Bureau of Standards
Gaithersburg, MD 20899

ABSTRACT

In the kraft recovery furnace, significant fuming of sodium takes place. It is essential to quantify the fuming rate because fume particles not only coat heat transfer tubes and plug flue gas passages but also act as SO_2 scavengers. An in-situ light scattering technique has been developed to measure fume particle size and number density from synthetic kraft smelt. This technique is based on the measured scattered light polarization ratio from fume particles. The multiangle measurements provide the necessary information on the imaginary part of the complex refractive index.

Results show that fume particle sizes can be correlated with a log-normal distribution function. The fume mean particle sizes vary from 0.23 to 0.30 μm and number density from 3×10^7 to 2×10^8 particles/cc.

Limited process studies showed that a higher nitrogen flow rate generates smaller fume particles, while a higher air flow rate generates larger fume particles. The effect of nitrogen flow rate on particle number density is opposite

---

Hsu is currently with Fluor Daniel, Pulp and Paper & Forest Products Engineering Division, Greenville, SC 29601.

that on the particle size. The effect of air flow rate on number density is insignificant. On balance, higher nitrogen flow rates produce higher fume mass density, but the effect of air flow rate on fume mass density is insignificant. The fuming rates determined here were less than those reported in the literature but showed a similar relationship between gas flow rate and fuming rate.

INTRODUCTION

The combustion of black liquor can be divided into four stages: drying, volatiles burning, char burning and smelt coalescence (1). During the char burning stage, significant fuming of sodium and potassium takes place. Fume particles form upon condensation of inorganic sodium and potassium salts from the vapor phase. Their sizes observed from the scanning electron microscope (SEM) picture, shown in Figure 1, range from 0.2 to 1 μm.

The sodium vapor in the gas stream reacts with CO_2 and O_2 to form Na_2CO_3 and subsequently with SO_2 and O_2 to form Na_2SO_4. Thus some level of fuming is essential to control SO_2 emission. The fume particles are recycled to the furnace via mixing with the fired liquor. This increases the inorganic content and reduces the fuel value of the fired black liquor (2). Fume particles are also detrimental, since they can coat heat transfer surface and reduce boiler efficiency. Together with carryover (entrained particles typically 0.1-1.0 mm), fume particles can contribute to plugging of flue gas passages. Plugging can lead to reduced capacity or shutdowns.

Figure 1 here

The cause of fume formation within the recovery boiler was once considered to be Na and NaOH vaporization which occurs at high temperature and reducing

conditions in the char bed (3,4). However, Borg et al. (3) reported that fuming also took place from the secondary air/liquor spray level. Fume also evolved during single particle burning (1). Clay et al. (5) and Cameron (6) discovered that copious quantities of sodium carbonate fume were formed when Na_2S was oxidized with air to Na_2SO_4 in a sodium carbonate melt.

Since fuming can occur under oxidative conditions, it may be possible to control the fuming rate by manipulating burning variables. In order to evaluate this possibility, an on-line fume sensor was needed. The objective of this work was to develop a nonintrusive fume sensor which can measure both fume particle size and number density within the gas stream, subsequently verifying that burning variables can affect particle size and number density. The particle number density is directly related to the fuming rate if both particle size and gas flow rate are determined. Determination of the particle size history with time may also provide supporting information on the fume formation mechanism.

THEORY

A large number of particle sizing instruments have been developed based on a variety of measurement principles. Among them, only imaging techniques, single particle counting techniques and ensemble techniques could be considered as likely nonintrusive techniques (7).

The imaging methods rely on freezing the image through the use of short duration light pulses. They have difficulty in determining particle sizes smaller than 5 μm because high quality small resolution lenses are hard to fabricate (8). The single particle technique measures individual particles as they pass through a focused laser beam. The particle size and number density is obtained through the information on individual particle counting (9,10,11). At present, these

techniques are limited to particle concentration less than or equal to 10^6 particles/cc and particle size greater than 0.3 μm.

The ensemble technique samples a large number of particles passing through a volume of space. The limitations on particle size and concentration are more relaxed in these techniques. The diffraction technique is applicable to the particle sizes between 1 and 1800 μm (12,13). The light scattering methods, including measurements of laser extinction/scattering (LES), scattering dissymmetry (SD) and polarization ratio of the scattered light (PR), with the aid of the Lorenz-Mie theory have been used to determine particle size in the range of 0.01 to 100 μm with particle concentration up to 10^{12} particles/cc (14-16).

Based on existing knowledge of the possible particle size (0.2 to 1 μm) and number density (above 10^6 particles/cc), the polarization-ratio technique with the Lorenz-Mie light scattering theory is used (15). The Lorenz-Mie theory (17) provides the differential scattering cross section, $C_{ij}(\theta,x,m)$, of a homogeneous spherical particle, where x is the size parameter ($x = \pi D/\lambda$), m is the complex refractive index ($m = n_1 + n_2\ \iota$, n_1 is the refractive index and n_2 is the absorption index), λ is the wavelength of the incident light and D is the particle diameter.

The subscripts i and j assume the letters v (vertical) or h (horizontal) according to whether the state of polarization of the scattered (i) and incident (j) radiation is perpendicular or parallel, respectively, to the plane of observation. For spherical particles of isotropic material, only i = j is of interest. A computer code developed by J. V. Dave at IBM is available to calculate the value of $C_{ii}(\theta,x,m)$ (18).

For the polydispersed particles such as fume, the mean cross section, $\overline{C}ii$ is needed. It is defined as

$$\overline{C}_{ii} = \int_0^\infty C_{ii}\, P(D)\, d\, D \qquad (1)$$

Thus a specific particle size distribution function, P(D), must be assumed to calculate the mean cross section. A two parameter logarithmic normal distribution function is used,

$$P(D) = \frac{1}{\sqrt{2\pi}\ D\ \sigma_g} \exp \left\{ - \left[\frac{\ln (D/Dg)}{\sqrt{2}\ \sigma_g} \right]^2 \right\} \qquad (2)$$

where Dg is the geometric mean diameter and σ_g is the geometric mean standard deviation. The size distribution function is normalized such that $\int_0^\infty P(D)\, dD = 1$.

The fume particle sizes in a preliminary test were first determined by the scanning electron microscope (SEM) and the image analyzer. The measured values were correlated with the log-normal distribution function and presented in Figure 2. The log-normal size distribution function fits the data with a correlation coefficient of 0.82. This is acceptable considering the limited sample in the SEM and the experimental errors in SEM and image analyzer measurements.

Figure 2 here

The intensity of light scattered by an ensemble of spherical particles of varying size, at a given scattering angle (θ), is determined from

$$Q_{ii}(\theta) = N\, \overline{C}_{ii}(\theta) \qquad (3)$$

where N is the particle number density (particles/cm^{-3}).

The polarization ratio, Γ, is further defined as

$$\Gamma(i) = \frac{Q_{hh}(i)}{Q_{vv}(i)} = \frac{\overline{C}_{hh}(i)}{\overline{C}_{vv}(i)} = \Gamma[\theta(i),\ m,\ \lambda,\ Dg,\ \sigma_g] \tag{4}$$

Since it is independent of particle number density, it can be related to particle diameter, Dg. Figure 3 illustrates the relationship at several detection angles. Thus the measured value of Γ can be used to determine the mean particle size, Dg, under a given specific scattering angle θ, known values of σ_g, λ, and m, and Γ is a monotonic function of Dg. After Dg is determined, $\overline{C}_{vv}(\theta)$ will be available from Eq. 1. Then the number density can be determined from the local value of Q_{vv} by Eq. 3.

Figure 3 here

To obtain the information on σ_g, λ, and m, several measurements of Γ and a nonlinear least square data fitting technique are needed. Eq. 4 can be further expressed as

$$\Gamma_j = \Gamma_j[x_1, x_2, \ldots\ldots, x_n; b_1, b_2, \ldots\ldots, b_n] \tag{5}$$

where j = 1 to m with n < m and the values of x represent the unknown variables, while the values of b represent the known parameters (14). Thus with several measurements of Γ at various detection angles, it is possible to determine best values of x_i which are appropriate for the measured Γ_j. The Levenberg-Marquart algorithm has been found to be very useful for this application (19).

In our system, the unknown variables are Dg, σ_g, and the imaginary part of the refractive index, n_2. The values of θ and λ are available from our optical system. The fume particle composition from the synthetic sodium salt melts is

mainly Na_2CO_3 (6). Thus the real part, n_1 in m for Na_2CO_3 is taken as 1.535 from the Handbook of Chemistry and Physics (20). To the authors' best knowledge, the value of n_2 is not available from the literature.

EXPERIMENTAL APPARATUS

The fume generation experiments are conducted by air introduction into synthetic sodium carbonate/sulfide melts. The experimental setup consisting of an electrical heated reactor and gas flow meters is shown in Figure 4. The ceramic reactor is normally charged with about 82 g of sodium carbonate and 5 to 14 g of sodium sulfide. These salts are mixed, added to the reactor and heated under a nitrogen purge to the reaction temperature, 940°C. The heating period takes about 100 minutes. Once the temperature was reached, air was added to the carrier gas to achieve the desired N_2/O_2 ratio. Insignificant fuming is observed during the nitrogen purge in comparison with the air/nitrogen purge.

Figure 4 here

The optical setup used for the light scattering measurements in the fume is shown in Figure 5 (20). A 4W argon ion laser operating at the 488 nm laser line with power at about 200 mW is the light source. The incident beam intensity is modulated using a mechanical chopper which operates at 1015 Hz. This frequency is used as a reference input for the lock-in amplifier to reject the noise at other frequencies and enhance signal quality. The beam passes through a polarized rotator which allows selection of the incident light polarization orientations.

Figure 5 here

The detection system consists of a polarization analyzer, collection optics and a photomultiplier tube (PMT) detector. A circular aperture (2.54 mm in diameter) placed in front of the collection optics defines the collection solid angle to be 2.6×10^{-5} sr (steradian). A pair of 250 mm lenses is used to focus the scattered light from the probe volume onto a 0.5 mm pinhole in front of the detector. The overall magnification of the collection optics is 0.5, thus providing a spatial resolution of 1 mm in the fuming. A narrow band interference filter centered at 488 nm is used for background rejection. The detection system is mounted on a movable carriage and two circular tracks. This allows continuous rotation of the optics about a fixed detection point over the range of 0 to 160 degrees. The output data from the lock-in amplifier are recorded by a microcomputer-based data acquisition system.

The scattered light detection system is calibrated to account for effects of the incident laser power, probe volume, light collection efficiency, detector sensitivity and electronic gain on the measurement. Propane gas with known Rayleigh scattering cross section was used for calibration (21,22). This allows for determination of the absolute value of the scattered light intensity, $Q_{ij}(\theta)$ $(m^{-1}sr^{-1})$ in direction θ per unit solid angle, per unit volume and per unit incident light.

EXPERIMENTAL RESULTS

When the laser beam passes through the generated fume stream, a scattered light pattern forms as shown in Figure 6. This indicates that a strong scattered light signal has been produced by the fume particles.

Figure 6 here

The value of n_2 was first determined from Γ measurements at several scattering angles. The reproduced small values of n_2 were obtained and shown in Table 1. This indicates that fume particles do not absorb the incident light, which is anticipated since their color is white. The n_2 value was assumed 0 for the future Mie calculation. The average Dg value, 0.233 μm, determined here was smaller than 0.301 μm observed from the SEM and the image analyzer. It is generally believed that the collection method, the SEM and image analyzer technique have a bias toward larger particles.

Table 1 here

The cross polarization effect which is significant when measured particles are not spherical was experimentally determined. Table 2 shows that the polarization effect on the Γ measurement is small (2% at θ = 100, 7% at θ = 110, and 6% at θ = 120). The cross polarization effect is even smaller on the Dg measurement (1% at both θ = 110 and θ = 120) mainly because the curve of Γ vs. Dg has a high slope, 12.7 at θ = 110 and 15.17 at θ = 120, at Dg from 0.20 to 0.25 μm. This is a confirmation that the shape of fume particles generated from our system is spherical.

Table 2 here

The experimental system was further used in limited tests to measure the fume particle size and number density under various reaction conditions. The empirical model

$$\text{Fume generation rate, g/min} = 161*(N_2,\ \text{L/min})^{0.907}*(O_2,\ \text{L/min})^{0.274} *\exp(-20{,}540\ \text{cal/mole}/RT) \quad (6)$$

developed by Cameron (6) shows that reaction temperature, nitrogen and oxygen flow rates will be important process variables of study. The effects of nitrogen and air flow rates on the fume particle size, number density and the fuming rate were studied. The particle size, Dg, was interpreted from Γ measurements at the detection angle, 110 degrees. The fume particle geometric standard deviation was assumed at 0.241, an average value of those reported in Table 1.

Figure 7 and Table 3 show that fume particles with smaller size are generated from the smelt at higher nitrogen flow rates when the oxygen flow rate is kept constant. The significance level for this relationship is above 99%. At a higher gas flow rate less retention time is allowed for particle growth. In addition, at a higher nitrogen flow rate the partial pressure of other gases, especially O_2, will be lowered. In the gas phase above the smelt surface, fume particles are formed by the following reaction.

$$1/2\ O_2 + CO_2 + 2\ Na \text{ -----> } Na_2CO_3$$

If the oxygen partial pressure is lower in the gas phase, sodium molecules will have fewer collisions with oxygen molecules. Cameron (6) showed that sodium vaporization rates increase with increasing nitrogen flow rates. The higher nitrogen flow lowered the Na partial pressure in the gas phase. This increased the mass transfer driving force for sodium vaporization from the melt. Data from the present work suggest that this increased vaporization occurs as smaller fume particles.

Figure 7 and Table 3 here

The effect of nitrogen flow rate on the particle number density is opposite that on the particle size. The dependence is significant at a level above 99%

(Figure 8 and Table 3). However, higher nitrogen flow rates still produce higher fume mass densities (Figure 9) even with finer particles, which is consistent with Cameron (6). The fume mass density is defined as $N \overline{V} \rho$ where:

N = particle number density, particles/cc

$\overline{V}$ = mean particle volume, cc/particle

$$\overline{V} = \int_0^\infty 4/3 \ \pi \ (D/2)^3 \ P(D) \ d \ D$$

ρ = density of Na_2CO_3, gm/cc.

Figures 8 and 9 here

Figure 10 and Table 4 show that higher air flow rates produce larger fume particles with a significance level above 99%. One possible explanation is that the effect of retention time on the particle size is overwhelmed by that of the oxygen partial pressure. The increased air or nitrogen flow reduces retention time, but only increased air flow maintains the same oxygen partial pressure. Another explanation is that the higher turbulence promoted more frequent early particle collisions.

Figure 10 and Table 4 here

The effects of air flow rate on both particle number density and fume mass density shown in Figures 11 and 12 are insignificant even if the significance level is chosen at 90%. As Cameron (6) points out, for the present contact mode, sulfide oxidation is gas side mass transfer limited. Also, oxygen consumption and the nitrogen flow rate are approximately inversely proportional. This means that as the nitrogen flow rate increases, the oxygen consumption rate decreases, and more oxygen is available to react with vaporized sodium. Therefore, more fume is generated, since reaction with oxygen lowers the partial

pressure of sodium in the gas phase. If both nitrogen and oxygen flows are simultaneously increased, no change in fuming rate is expected.

Figures 11 and 12 here

The particle number densities observed in Table 4 are lower than in Table 3. This likely resulted from different positions of measured fume volumes. The measured fume volume in Table 4 was farther downstream from the furnace than that in Table 3. The ambient air dilutes the fume stream as it continues downstream of the furnace.

The fuming rate is estimated by

$$\text{Fuming rate} = N \overline{V} \rho F_{gt} \tag{7}$$

where: F_{gt} = total gas flow rate at gas exit temperature, cc/min.

The effects of nitrogen and air flow rates on the measured fuming rates by Eq. 7 and predicted by Eq. 6 are shown in Figures 13 and 14. The gas temperature was measured by a thermocouple inserted into the fume stream at the exit of the furnace. It is interesting to see that in both figures the measured values are always smaller than the model prediction but with the same trend of the gas flow rate effect on the fuming rate.

Figures 13 and 14 here

The lower measured fuming rate by Eq. 7 could result from the dispersion effect that has diluted the fume particle number density in the fume stream at the exit of the furnace. In addition, the fume particle number density is not expected to be uniform in the fume stream. Thus the fuming rate determined by Eq. 7 could be only an approximation for the given experimental system.

CONCLUSIONS

A nonintrusive laser-polarization-ratio technique to measure the fume particle size and number density has been successfully demonstrated. It also verifies that fume particle size and number density can be affected by the burning variables such as nitrogen and air flow rates. Significant conclusions are summarized as follows:

1. The fume particle sizes determined by the SEM and the image analyzer can be correlated with a log-normal distribution function with a correlation coefficient, 0.82.

2. Several measurements of polarization ratio, Γ, provide us with the information on Dg, σ_g and n_2.

3. The fume mean particle size, 0.23 μm was smaller than 0.30 μm that was measured by the SEM and the image analyzer.

4. A higher nitrogen flow rate generates smaller fume particles, but a higher air flow rate generates larger fume particles. The effect of nitrogen flow rate on particle number density is opposite that on the particle size, while the effect of air flow rate is insignificant. In summary, higher nitrogen flow rates produce higher fume mass densities with finer particles, but the effect of air flow rate on fume mass density is insignificant.

5. The fuming rates determined here were less than those reported in the literature but showed a similar relationship between flow rate and fuming rate.

This technique will be used to measure the fume particle size and number density generated within the IPC black liquor process flow reactor (23).

ACKNOWLEDGMENTS

The contributions of Mr. Orlin G. Kuehl at IPC for construction of the fume generation system and Mrs. Kristi Blythe at Appleton Papers Inc. for measuring the fume particle sizes by the image analyzer are acknowledged. We appreciated the assistance of Dr. Andrej Macek and Mr. James Allen of the National Bureau of Standards in the optical system of this work. This work was funded by the Department of Energy Office of Industrial Programs, Stanley F. Sobczynski Program Manager. Partial funding was also obtained from The American Paper Institute, Recovery Boiler R&D Subcommittee.

LITERATURE CITED

1. Solin, P., M. Hupa, and P. Hyoty. "Combustion Behavior of Black Liquor Droplets." Presented at 1985 International Chemical Recovery Conference, New Orleans, LA, May, 1985, p. 335.

2. Cameron, J. H., D. T. Clay, and T. M. Grace. "Oxidative Fuming - The Phenomena and Possible Interpretations." TAPPI Proc: 1985 International Chemical Recovery Conference, p. 435.

3. Borg, A., A. Teder, and B. Warnqvist, Tappi 57(1):126(1974).

4. Warnqvist, B., Svensk Papperstid. 76(12):463(1973).

5. Clay, D. T., T. M. Grace and R. J. Kapheim. "Fume Formation from Synthetic Sodium Salt Melts and Commercial Kraft Smelts." AIChE Symposium, 1984, p. 99.

6. Cameron, J. H. "Reaction Enhanced Vaporization of Molten Salt." Chem. Eng. Comm. 59:243-57(1987).

7. Presser C., A. K. Gupta, R. J. Santoro and H. G. Semerjian, "Laser Diagnostics for Characterization of Fuel Sprays." Proc. ICALEO 86, Arlington, VA, November 10-13, 1986.

8. Bachalo, W. D. "Droplet Analysis Techniques: Their Selection and Applications." Liquid Particle Size Measurement Techniques, ASTM STP 848, American Society for Testing and Materials, 1984, p. 5-21.

9. Farmer, W. M. "Measurement of Particle Size, Number Density and Velocity Using a Laser Interferometer." Applied Optics 11(11):2603(1972).

10. Bachalo, W. D. and M. J. Houser. "Phase/Doppler Spray Analyzer for Simultaneous Measurements of Drop Size and Velocity Distributions." Optical Engineering, 23(5):583(1984).

11. Holve, D. J. and Annen, K. D. "Optical Particle Counting, Sizing, and Velocimetry Using Intensity Deconvolution." Optical Engineering, 23(5): 591(1984).

12. Dobbins, R., L. Crocco and I. Glassman. "Measurement of the Mean Particle Sizes of Sprays from Diffractively Scattered Light." AIAA J. 1:1882(1963).

13. Cornillault, J. "Particle Size Analyzer." Applied Optics 11(2):265(1972).

14. Dobbins, R. A., R. J. Santoro, and H. G. Semerjian. "Interpretation of Optical Measurements of Soot in Flames, in Combustion Diagnostics by Nonintrusive Methods." Prog. Astro. and Aero., 92:208(1984).

15. Presser, C., A. K. Gupta, R. J. Santoro and H. G. Semerjian. "Droplet Size Measurements in a Kerosene Spray Flame." Proc. ICLASS-85, held at Imperial College, London, p. VIIC/2/1-13, July, 1985.

16. Presser, C., A. K. Gupta, R. J. Santoro, and H. G. Semerjian. "Velocity and Droplet Size Measurements in a Fuel Spray, Paper No. 86-0297, Presented at the AIAA 24th Aerospace Sciences Meeting, Reno, NV, January, 1986.

17. Van de Hulst, H. C. "Light Scattering by Small Particles." John Wiley and Sons, New York, 1957.

18. Dave, J. V. "Subroutines for Computing the Parameters of the Electromagnetic Radiation Scattered by a Sphere." Report 320-3237, IBM Palo Alto Scientic Center, Palo Alto, CA, May, 1968.

19. More, J. J. "The Levenberg-Marquardt Algorithm: Implementation and Theory. Numerical Analysis, Lecture Notes in Mathematics, V. 630, edited by G. A. Wilson, Springer-Verlag, New York, 1977, p. 105.

20. CRC, Handbook of Chemistry and Physics, 59th edition, CRC Press, West Palm Beach, FL, 1979.

21. Rudder, R. R. and D. R. Bach. "Rayleigh Scattering of Ruby-Laser Light by Neutral Gases." Journal of the Optical Society of America 58(9):1260 (1968).

22. Bogaard, M. P., A. D. Buckingham, R. K. Pierens, and A. H. White. "Rayleigh Scattering Depolarization Ratio and Molecular Polarizability Anisotropy for Gases." Journal of the Chemical Society, Faraday Transactions I, 74:3008(1978).

23. Clay, D. T., et al. Fundamental Studies of Black Liquor Combustion, Report No. 2 - Phase 1. Report to the U.S. Dept. of Energy, Office of Industrial Programs. Contract No. DE-AC02-83CE40637, January, 1987.

Figure Captions

Figure 1. Fume particles observed with a scanning electron microscope. The bar dimension is one micron.

Figure 2. Comparison between model prediction and experimental data. N = number of particles counted. Dg = geometric mean diameter, microns. σg = geometric mean standard deviation.

Figure 3. Relationship between polarization ratio and geometric mean diameter.

Figure 4. Fume generation system.

Figure 5. Experimental apparatus for laser scattering measurements.

Figure 6. Scattered light pattern by fume particles.

Figure 7. Nitrogen flow rate effect on fume particle size. Reactor condition, T: 940 C, oxygen: 0.021 L/min.

Figure 8. Nitrogen flow rate effect on fume particle number density. Reactor condition, T: 940 C, oxygen: 0.021 L/min.

Figure 9. Nitrogen flow rate effect on fume mass density. Reactor condition, T: 940 C, oxygen: 0.021 L/min. $F_o = 21.4 > F_{0.01,2,9} = 8.02$.

Figure 10. Air flow rate effect on fume particle size. Reactor condition, T: 940 C, nitrogen: 0.1 L/min.

Figure 11. Air flow rate effect on fume particle number density. Reactor condition, T: 940 C, nitrogen: 0.1 L/min.

Figure 12. Air flow rate effect on fume mass density. Reactor condition, T: 940 C, nitrogen: 0.1 L/min. $F_o = 1.18 < F_{0.01,2,9} = 8.02$.

Figure 13. Nitrogen flow rate effect on fuming rate. Reactor condition, T: 940 C, oxygen: 0.021 L/min.

Figure 14. Air flow rate effect on fuming rate. Reactor condition, T: 940 C, nitrogen: 0.1 L/min.

Table 1. Determination of Dg, σg, and N_2 through Γ measurements at several detection angles.

	θ (degs)	Γ measurements	Γ (average)	
First	90	0.58, 0.60, 0.61	0.60	Dg = 0.235 μm
test	105	0.68, 0.73, 0.69	0.70	σ_g = 0.259
	120	0.93, 0.94	0.94	n_2 = 0.00005
	130	1.11, 1.13, 1.16	1.13	
Second	90	0.41, 0.44, 0.38, 0.42	0.41	Dg = 0.232 μm
test	100	0.47, 0.46	0.46	σ_g = 0.223
	110	0.63, 0.62	0.62	n_2 = 0.0003
	120	0.80, 0.79	0.79	

Reactor conditions: T : 940 C, N_2 : 0.8 L/min,
air : 0.1 L/min.

Table 2. Cross polarization effect on Γ and Dg measurements.

θ (degs)	Q_{hh}	Q_{vv}	Q_{hv}	Q_{vh}	$\Gamma\left(\frac{Q_{hh}}{Q_{vv}}\right)$	Dg (μm)	$\Gamma\left(\frac{Q_{hh}+Q_{hv}}{Q_{vv}+Q_{vh}}\right)$	Dg (μm)
90	0.0061	0.0150	0.0004	0.0007	0.41	0.217	0.41	0.217
100	0.0149	0.0318	0.0009	0.0022	0.47	0.222	0.46	0.222
110	0.0068	0.0107	0.0004	0.0014	0.64	0.230	0.60	0.227
120	0.0089	0.0111	0.0004	0.0014	0.80	0.231	0.75	0.228

Reactor conditions : T : 940 C, N_2 : 0.8 L/min,
air : 0.1 L/min.
unit of Q_{ij}, i,j = v,h : particles/cm.

Table 3. Nitrogen flow rate effect on Dg and N measurements.

N_2 (L/min)	Dg ± Std. Dev. (μm)	N ± Std. Dev. (particles/cc)
0.579	0.244 ± 0.002	1.94 ± 0.08 x 10^8
0.279	0.249 ± 0.002	1.37 ± 0.18 x 10^8
0.079	0.277 ± 0.012	0.96 ± 0.13 x 10^8

$F_0 = 24.4 > F_{0.01,2,9} = 8.02$ for D_g
$F_0 = 52.2 > F_{0.01,2,9} = 8.02$ for N
Reactor condition : T : 940 C
O_2 : 0.021 L/min.

Table 4. Air flow rate effect on Dg and N measurements.

Air (L/min)	Dg ± Std. Dev. (μm)	N ± Std. Dev. (particles/cc)
0.5	0.300 ± 0.018	$3.78 \pm 1.16 \times 10^7$
0.3	0.279 ± 0.011	$4.64 \pm 0.65 \times 10^7$
0.1	0.264 ± 0.002	$4.97 \pm 0.15 \times 10^7$

$F_0 = 9.1 > F_{0.01,2,9} = 8.02$ for D_g
$F_0 = 2.5 < F_{0.1,2,9} = 3.01$ for N
Reactor condition : T : 940 C
N_2 : 0.1 L/min.

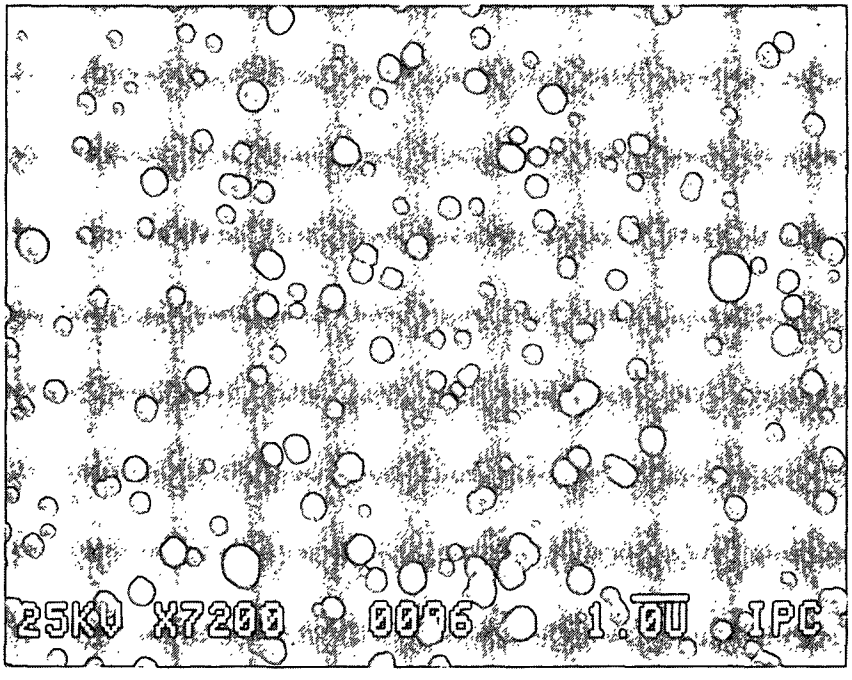

Figure 1. Fume particles observed with a scanning electron microscope. The bar dimension is one micron.

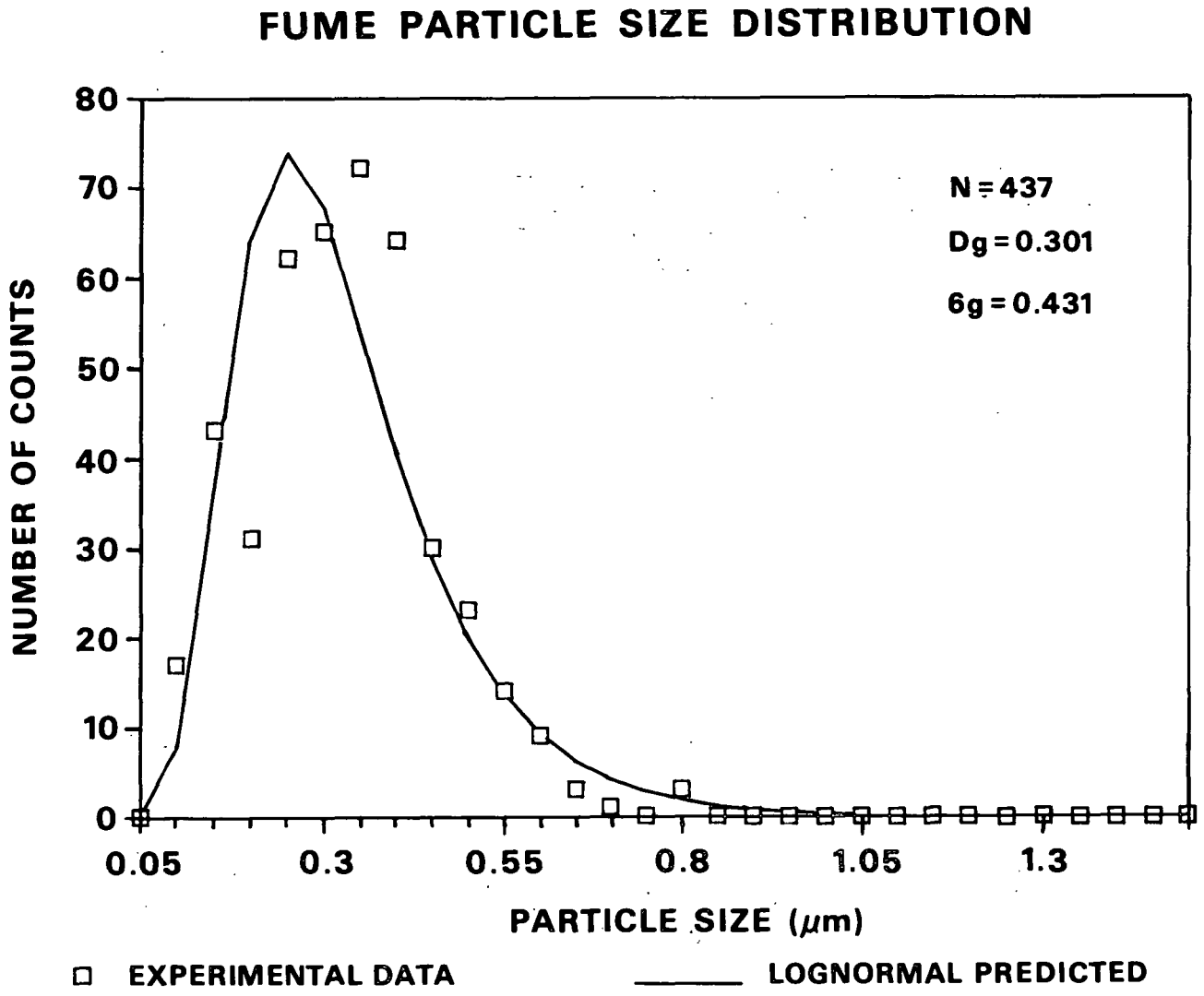

Figure 2. Comparison between model prediction and experimental data. N = number of particles counted. Dg = geometric mean diameter, microns. σg = geometric mean standard deviation.

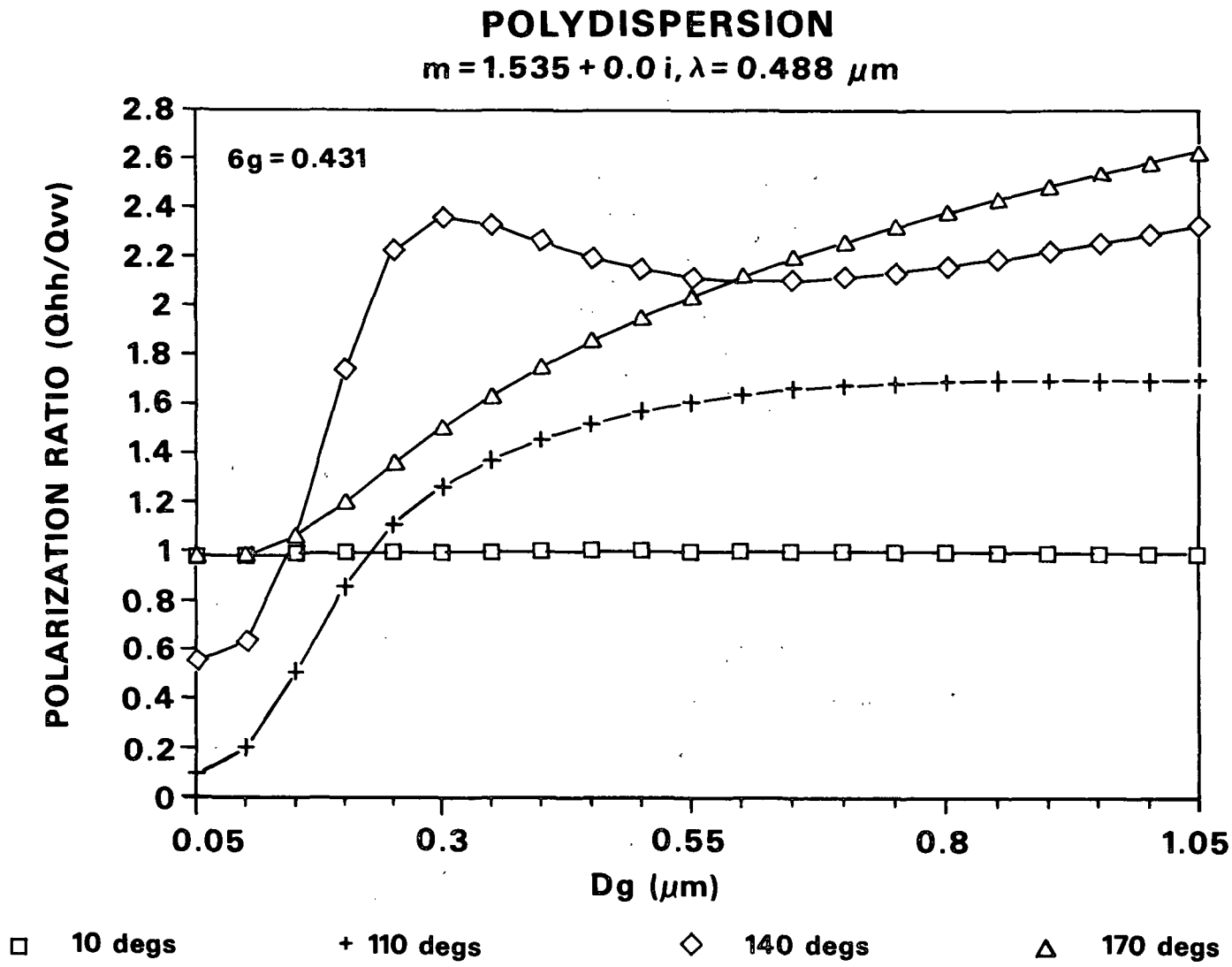

Figure 3. Relationship between polarization ratio and geometric mean diameter.

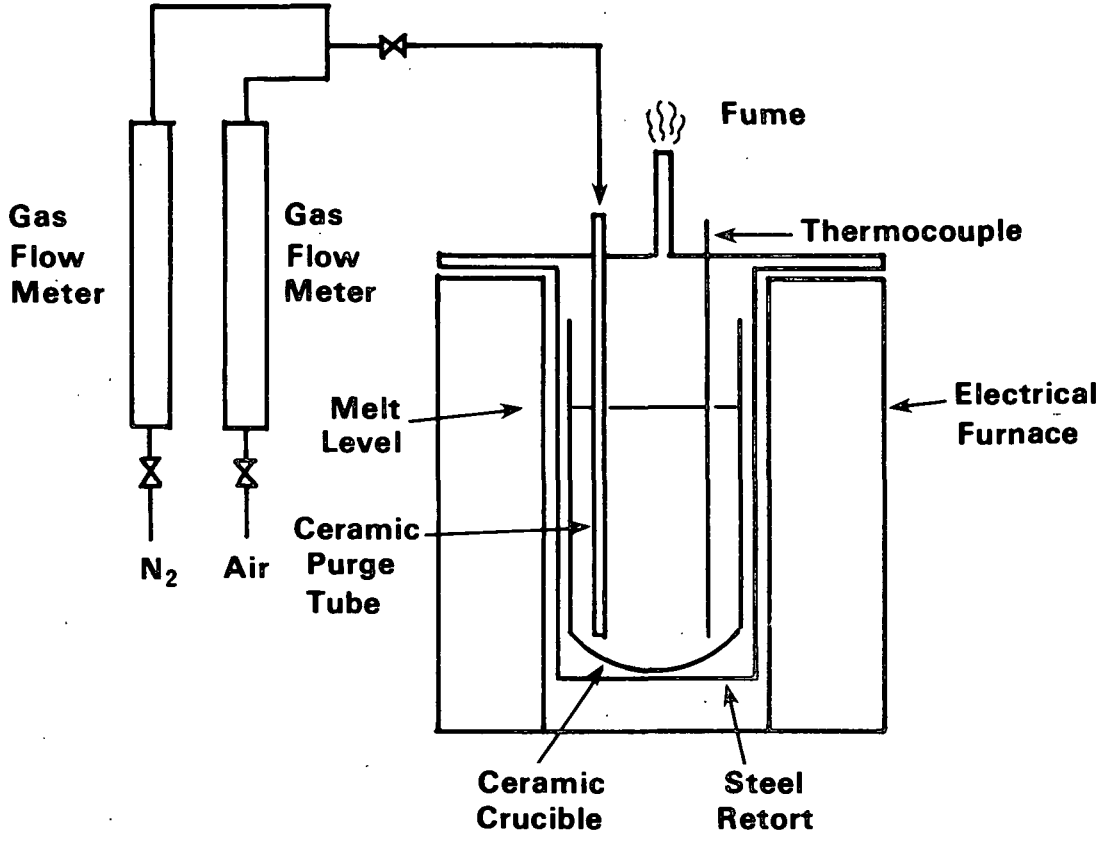

Figure 4. Fume generation system.

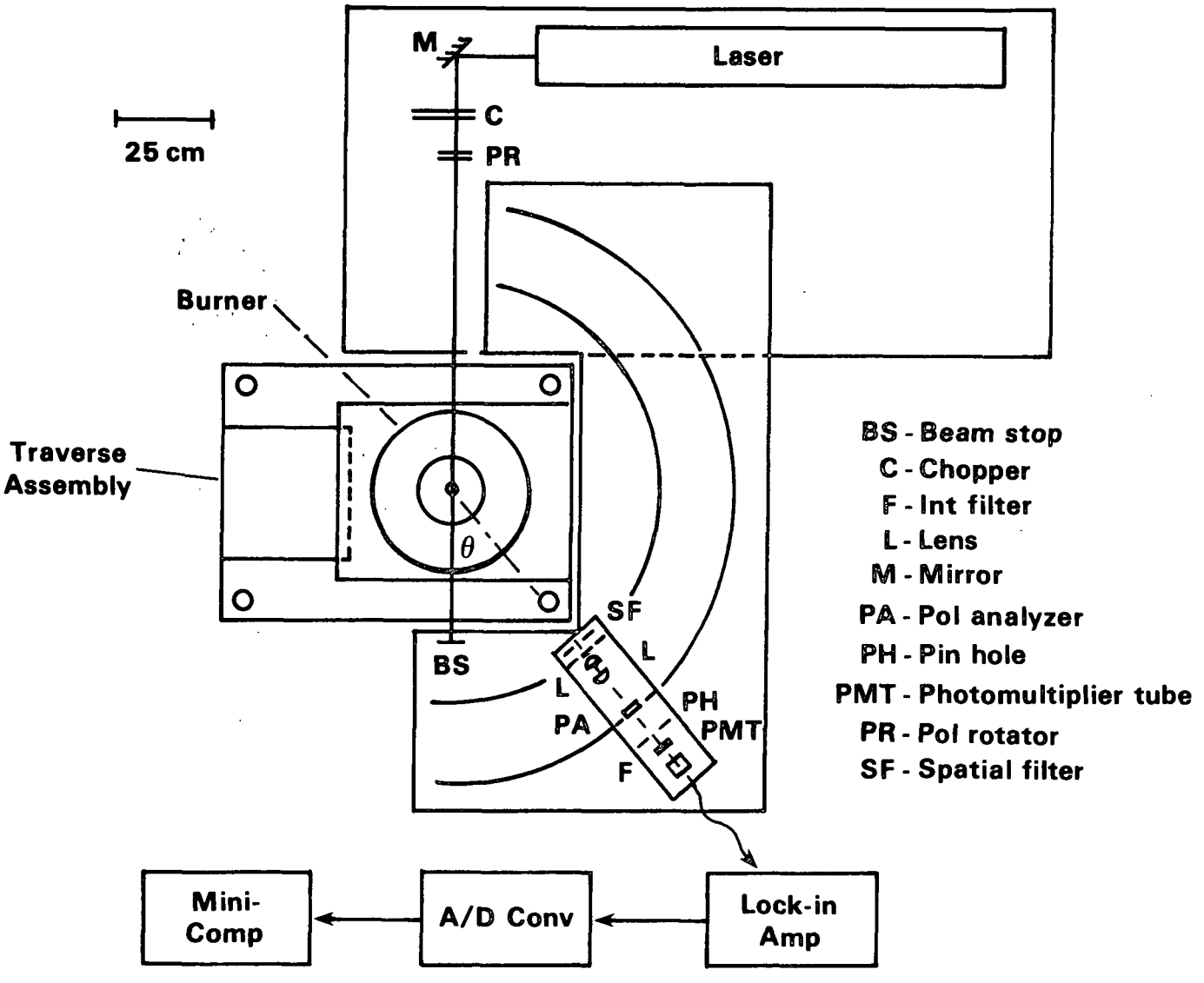

Figure 5. Experimental apparatus for laser scattering measurements.

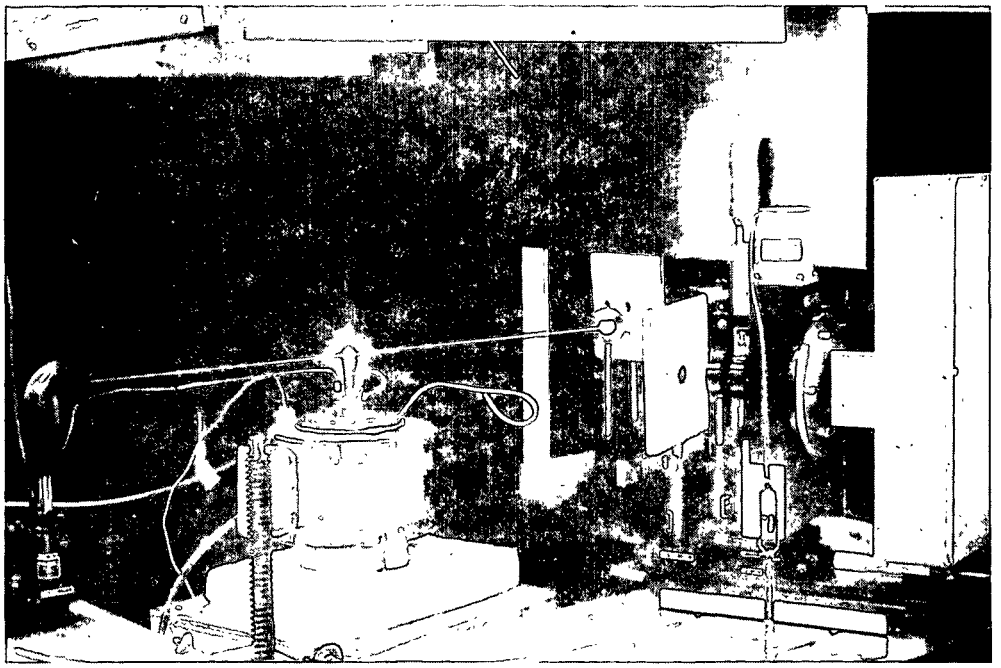

Figure 6. Scattered light pattern by fume particles.

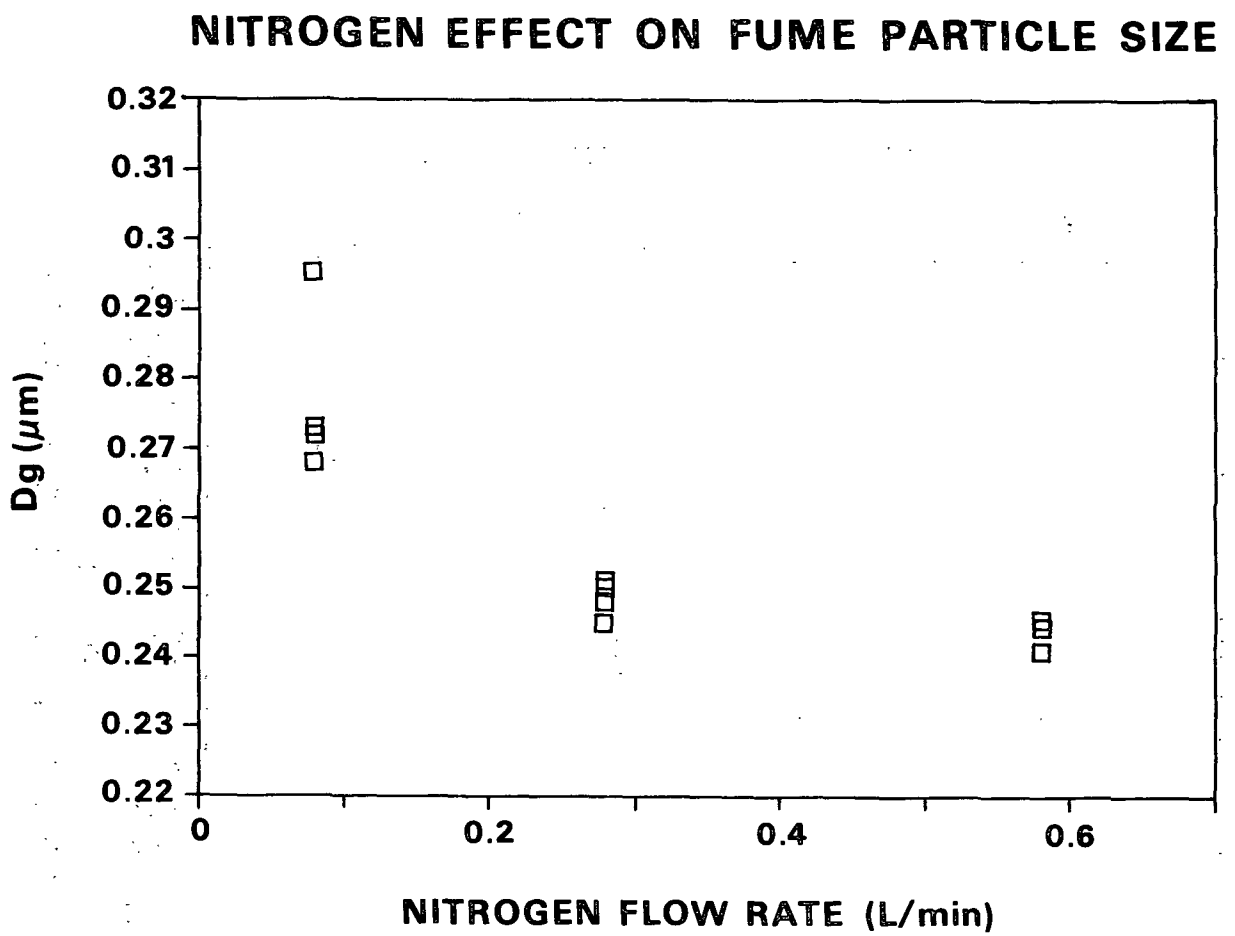

Figure 7. Nitrogen flow rate effect on fume particle size. Reactor condition, T: 940 C, oxygen: 0.021 L/min.

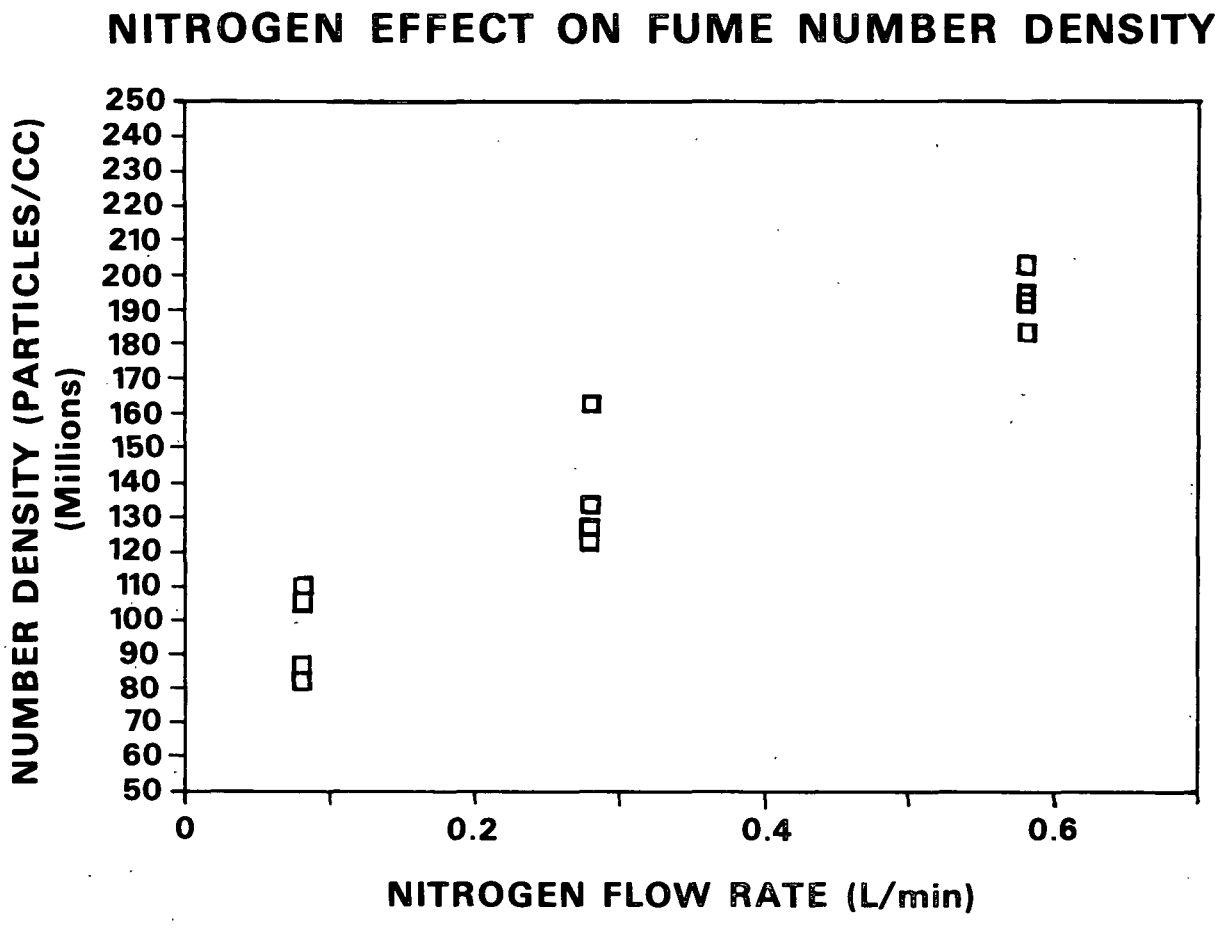

Figure 8. Nitrogen flow rate effect on fume particle number density. Reactor condition, T: 940 C, oxygen: 0.021 L/min.

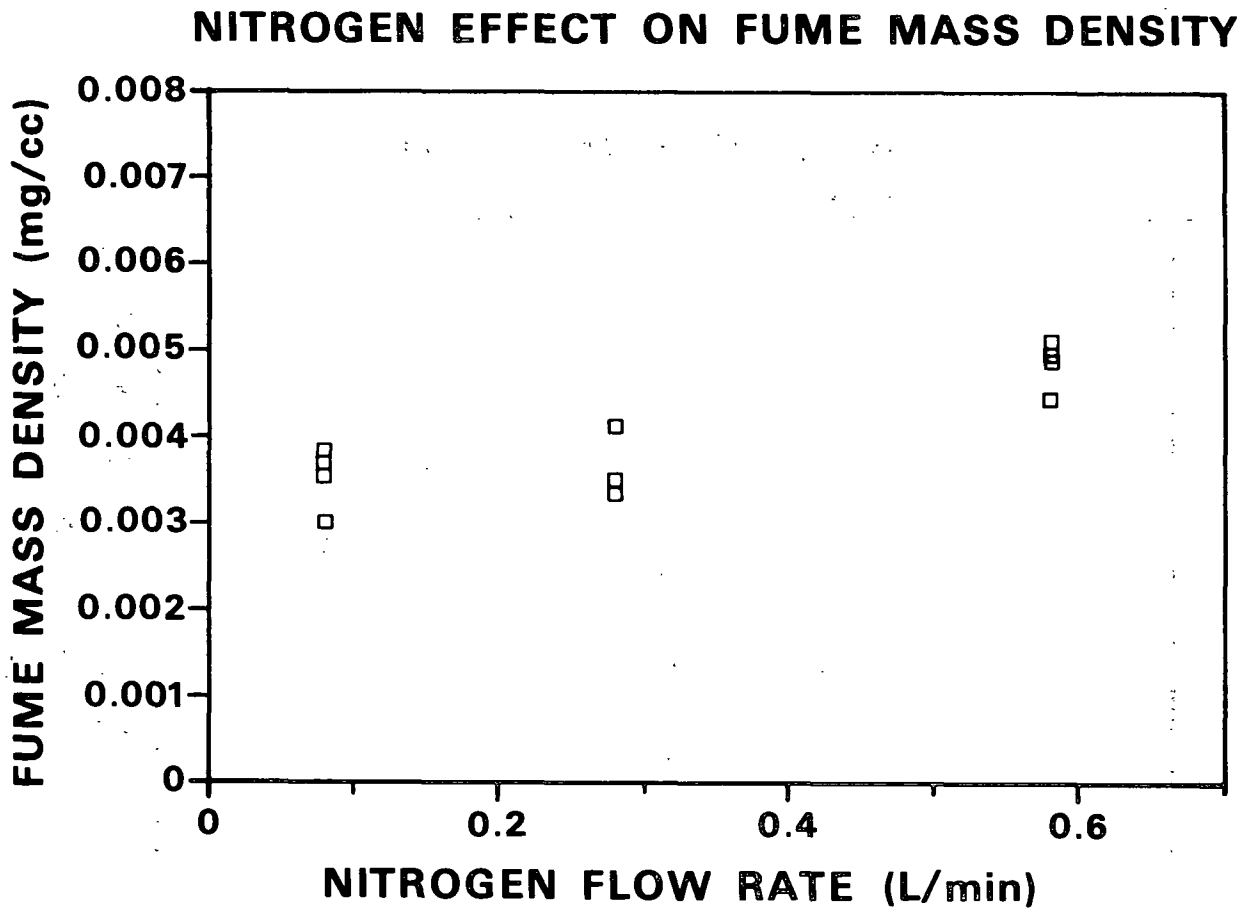

Figure 9. Nitrogen flow rate effect on fume mass density. Reactor condition, T: 940 C, oxygen: 0.021 L/min. $F_o = 21.4 > F_{0.01,2,9} = 8.02$.

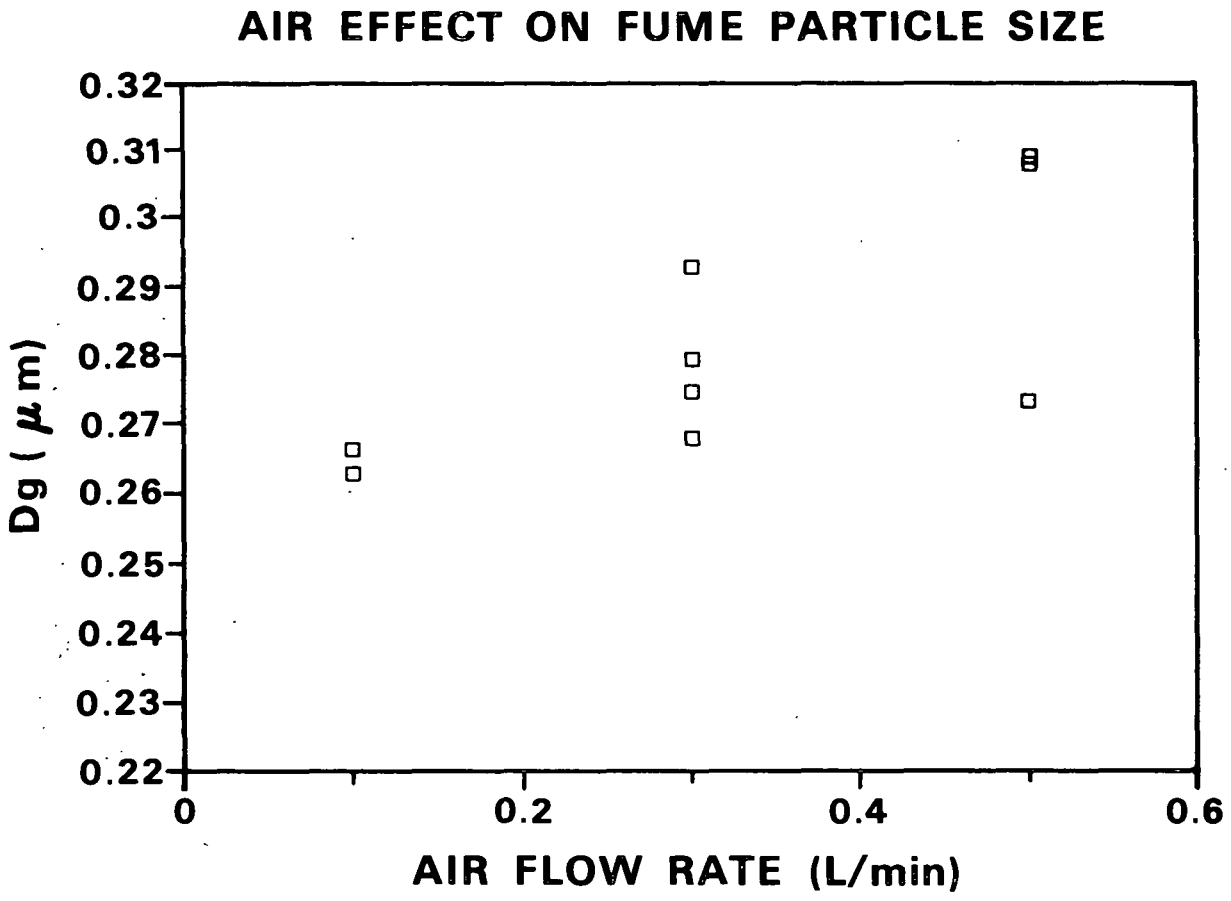

Figure 10. Air flow rate effect on fume particle size.
Reactor condition, T: 940 C, nitrogen: 0.1 L/min.

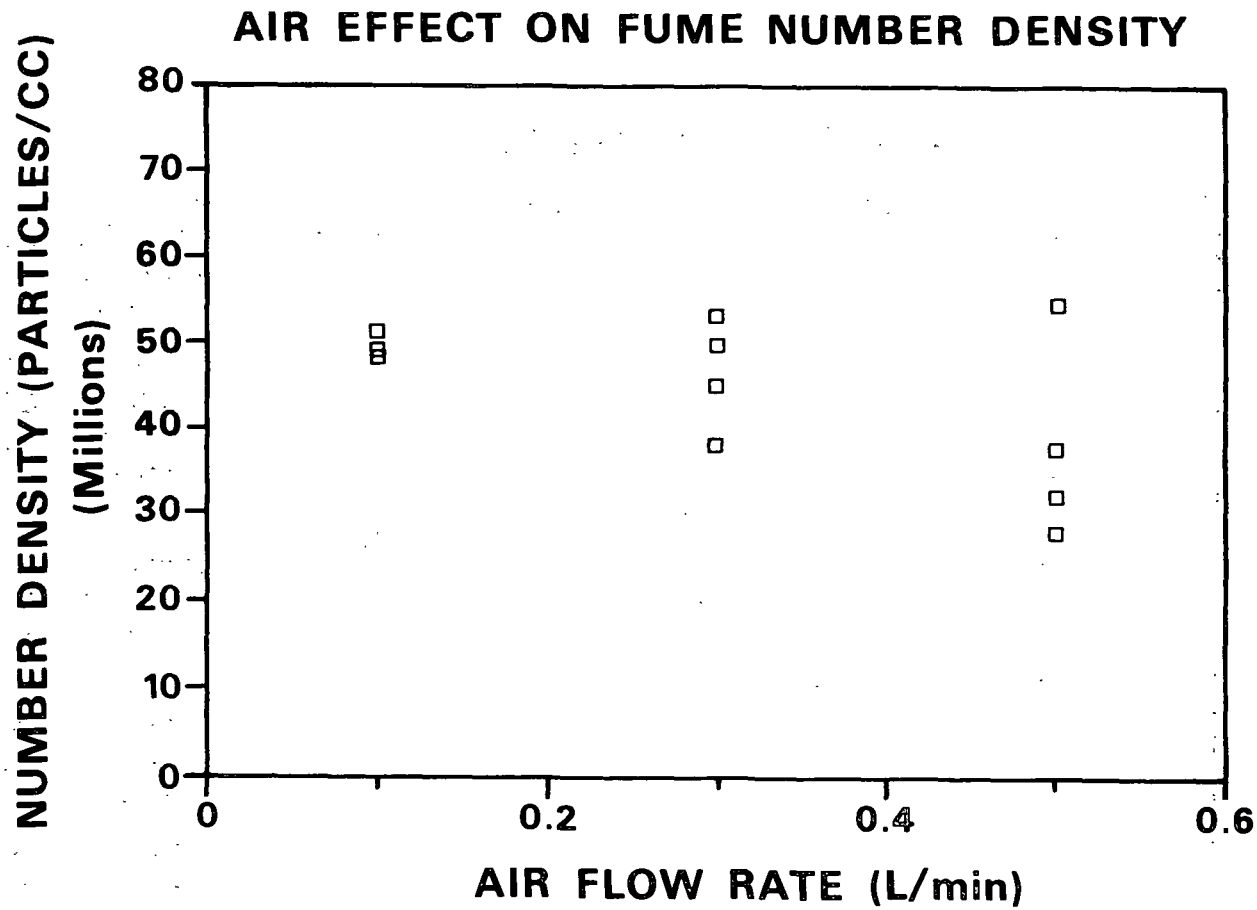

Figure 11. Air flow rate effect on fume particle number density. Reactor condition, T: 940 C, nitrogen: 0.1 L/min.

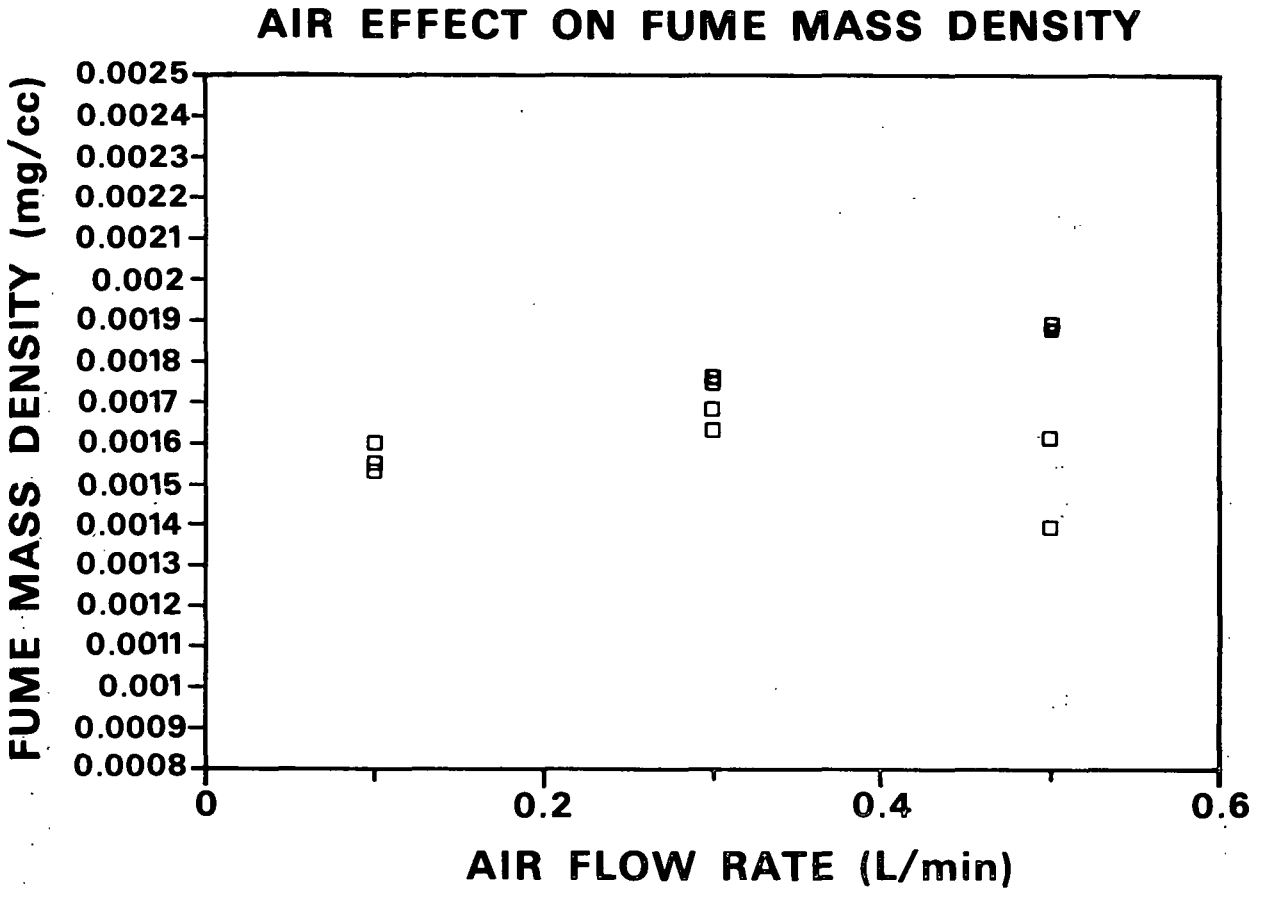

Figure 12. Air flow rate effect on fume mass density.
Reactor condition, T: 940 C, nitrogen: 0.1 L/min.
$F_o = 1.18 < F_{0.01,2,9} = 8.02$.

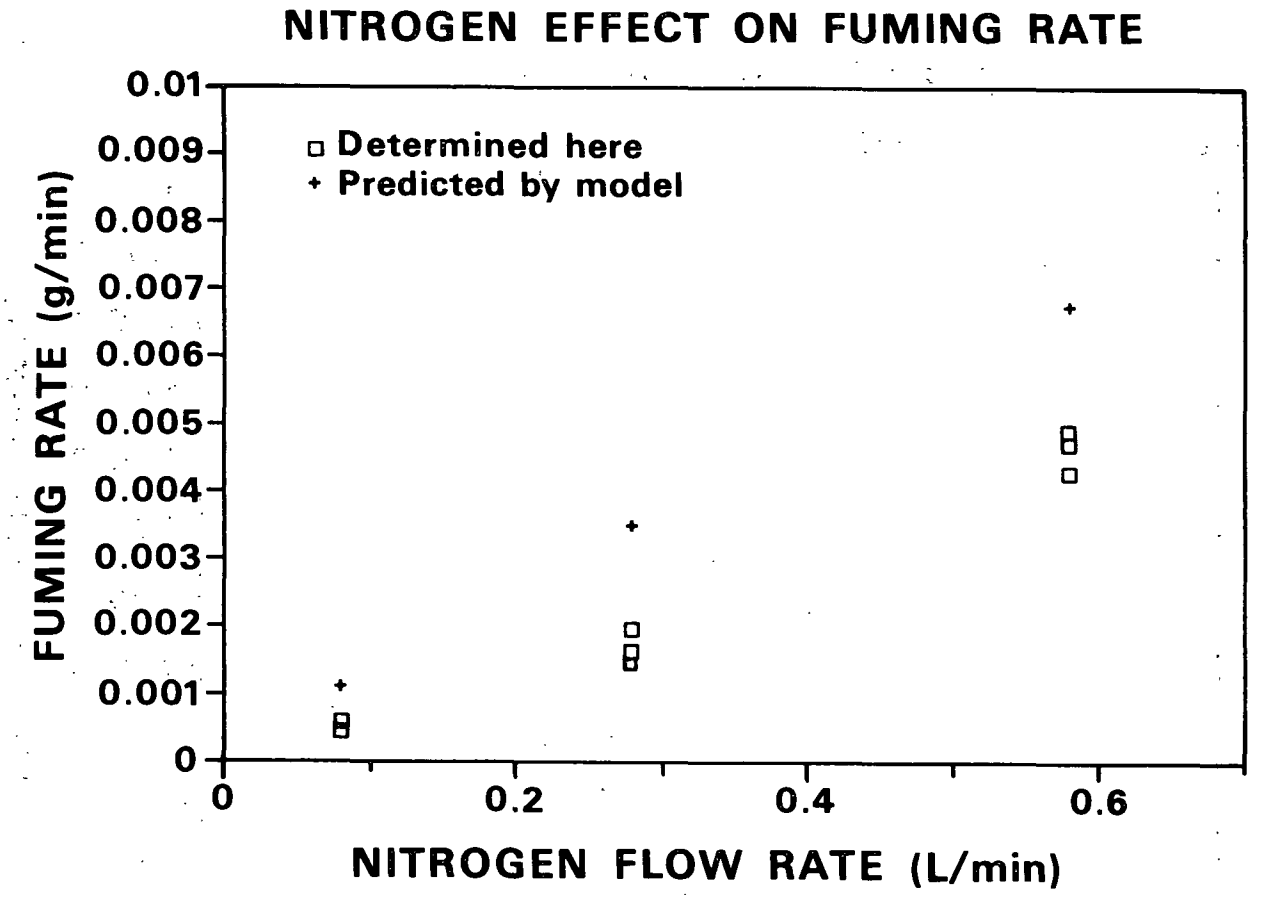

Figure 13. Nitrogen flow rate effect on fuming rate.
Reactor condition, T: 940 C, oxygen: 0.021 L/min.

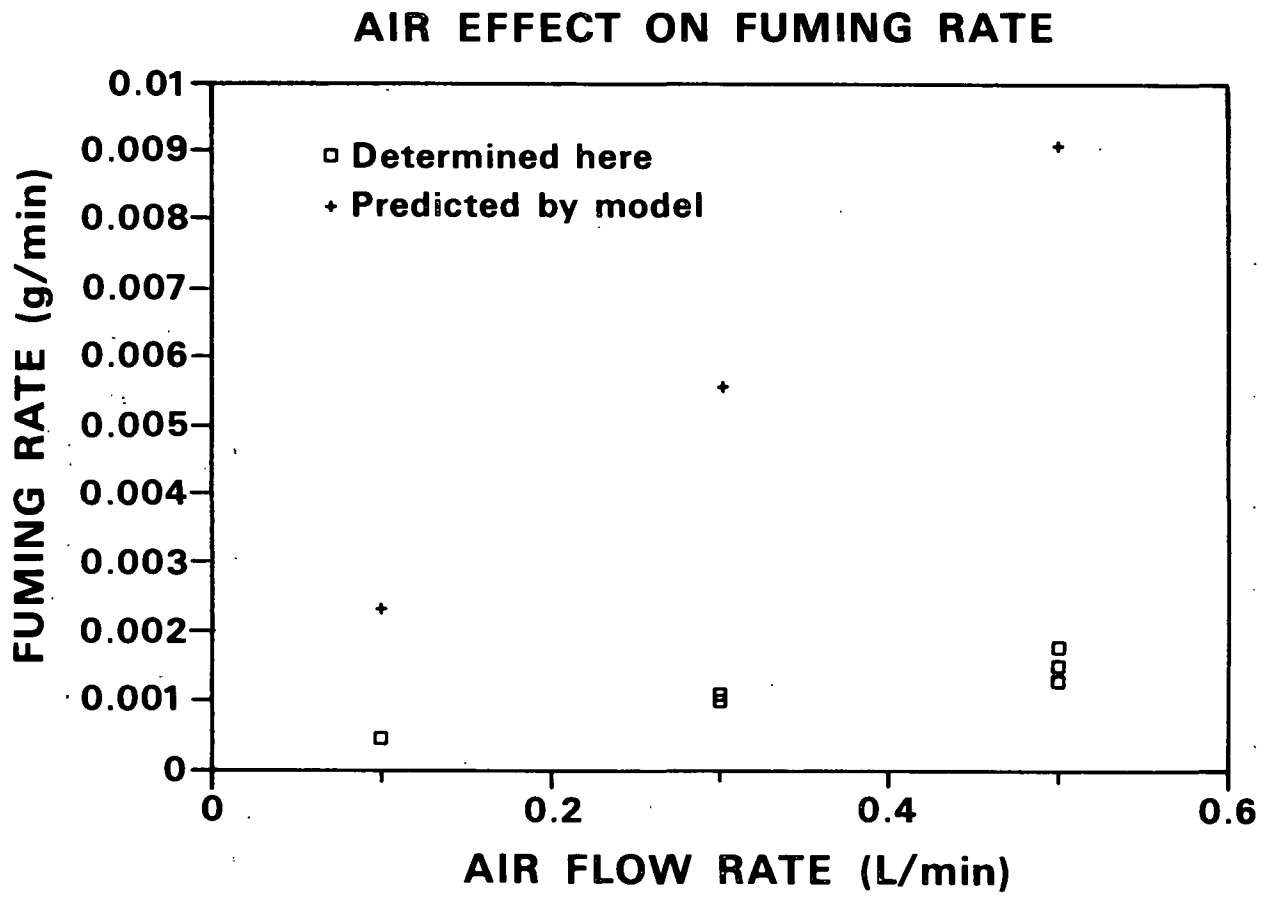

Figure 14. Air flow rate effect on fuming rate.
Reactor condition, T: 940 C, nitrogen: 0.1 L/min.